NANO · MICRO small
www.small-journal.com

A MXene-Based Wearable Biosensor System for High-Performance In Vitro Perspiration Analysis

*Yongjiu Lei, Wenli Zhao, Yizhou Zhang, Qiu Jiang, Jr-Hau He, Antje J. Baeumner, Otto S. Wolfbeis, Zhong Lin Wang, Khaled N. Salama, and Husam N. Alshareef**

Wearable electrochemical biosensors for sweat analysis present a promising means for noninvasive biomarker monitoring. However, sweat-based sensing still poses several challenges, including easy degradation of enzymes and biomaterials with repeated testing, limited detection range and sensitivity of enzyme-based biosensors caused by oxygen deficiency in sweat, and poor shelf life of sensors using all-in-one working electrodes patterned by traditional techniques (e.g., electrodeposition and screen printing). Herein, a stretchable, wearable, and modular multifunctional biosensor is developed, incorporating a novel MXene/Prussian blue ($Ti_3C_2T_x$/PB) composite designed for durable and sensitive detection of biomarkers (e.g., glucose and lactate) in sweat. A unique modular design enables a simple exchange of the specific sensing electrode to target the desired analytes. Furthermore, an implemented solid–liquid–air three-phase interface design leads to superior sensor performance and stability. Typical electrochemical sensitivities of 35.3 μA mM^{-1} cm^{-2} for glucose and 11.4 μA mM^{-1} cm^{-2} for lactate are achieved using artificial sweat. During in vitro perspiration monitoring of human subjects, the physiochemistry signals (glucose and lactate level) can be measured simultaneously with high sensitivity and good repeatability. This approach represents an important step toward the realization of ultrasensitive enzymatic wearable biosensors for personalized health monitoring.

1. Introduction

Wearable electronics are devices that can be worn or mated with human skin to continuously and closely monitor an individual's activities, including respiration rate, heart rate, electrocardiograms, skin temperature, and bodily motion.[1–3] Wearable electrochemical biosensors that are based on sweat analysis present a promising means for noninvasive biomarker monitoring. Moreover, recent advances in wearable sweat sensors have produced devices that can measure sweat metabolites, such as glucose, lactate, and alcohol, as well as electrolytes, including sodium and potassium ions, and pH.[4–13] However, sweat-based sensing still poses several challenges. For example, most wearable biosensor devices are prepared by the all-in-one architecture patterned by traditional techniques (e.g., electrodeposition and screen printing). This configuration inevitably results in poor shelf life of the whole sensor patch because of rapid deactivation of enzymes and biomaterials upon repeated testing.[5–9] On the other hand, the sensitivity and stability of sweat biosensors are of great challenge as a consequence of the high resistance of the substrate and the oxygen-deficiency problem.[9] In addition, mechanical friction and deformation of devices on the soft human skin can delaminate the enzyme layer from the biosensor and cause mechanical failure of the wearable devices. Given these issues, advanced construction design for wearable sweat biosensors with enhanced sensitivity and stability is needed.

Large-area graphene films, synthesized by a chemical vapor deposition (CVD) process, enable many applications including large-scale flexible and stretchable electronics.[14] However, the low density of electrochemically active defects in CVD-synthesized graphene limits its application in biosensing.[8,9] Recently, a new class of 2D nanomaterials, namely, MXene, synthesized by etching out the A layers from the layered $M_{n+}AX_n$ phases, has emerged as a promising graphene analog. There are more than 70 known $M_{n+1}AX_n$ or MAX phases, indicating that numerous MXenes of varying compositions could be explored.[15–17] MXene's rich chemistries and unique 2D morphologies[18] have sparked intense interest in the exploitation of MXenes for energy storage,[19–22] catalysis,[23] conductive reinforcement additives,[24,25] and chemical sensing.[26,27] As a typical case in MXene family, $Ti_3C_2T_x$ MXene has metallic conductivity

Dr. Y. Lei, Dr. W. Zhao, Dr. Y. Zhang, Dr. Q. Jiang, Prof. H. N. Alshareef
Materials Science and Engineering Physical Science and Engineering Division
King Abdullah University of Science and Technology (KAUST)
Thuwal 23955-6900, Saudi Arabia
E-mail: husam.alshareef@kaust.edu.sa
Prof. J.-H. He, Prof. K. N. Salama
Computer, Electrical and Mathematical Science and Engineering Division
King Abdullah University of Science and Technology (KAUST)
Thuwal 23955-6900, Saudi Arabia
Prof. A. J. Baeumner, Prof. O. S. Wolfbeis
Institute of Analytical Chemistry
Chemo- and Biosensors
University of Regensburg
Universitaetsstrasse 31, 93053 Regensburg, Germany
Prof. Z. L. Wang
School of Materials Science and Engineering
Georgia Institute of Technology
Atlanta, GA 30332-0245, USA
The ORCID identification number(s) for the author(s) of this article can be found under https://doi.org/10.1002/smll.201901190.

DOI: 10.1002/smll.201901190

and shows amazing electrochemical activity, which could be highly beneficial in sensor development for various diagnostic purposes.[26,28–30] The unique 2D morphology and high biocompatibility of $Ti_3C_2T_x$ drive great motivation to design advanced nanohybrid systems with bioreceptors like antigen–antibody, proteins, cells, and enzymes.[31] $Ti_3C_2T_x$ acts as sensitive detection interface that allows facile immobilization of biomolecules for designing highly advanced detection systems and exploiting their utilization in analytical chemistry.[32,33] Nonetheless, achieving the desired signal-to-noise ratio and stability for such sensors, especially for in situ detection, remains highly challenging.

Given that all oxidase-based biosensors (e.g., glucose oxidase, lactate oxidase, alcohol oxidase, and cholesterol oxidase) consume oxygen,[34–37] enhanced O_2-containing environment is required. Conventional biosensors are based on electrodes with a solid–liquid two-phase interface. Hence, oxygen that is required at the enzymatic reaction zone is supplied through a liquid phase with a low diffusion coefficient compared to that of oxygen in the air, which restricts the upper detection limit of linearity, sensitivity, and accuracy according to Fick's law of diffusion.[38,39]

This study presents a stretchable, wearable, and modular multifunctional biosensing system for the simultaneous and highly selective screening of a panel of biomarkers in sweat. 2D MXene ($Ti_3C_2T_x$) nanosheets are first introduced in an oxygen-rich enzyme biosensor. The working electrode design is based on the use of a $Ti_3C_2T_x$/PB composite that is combined with a hydrophobic substrate and has a solid–liquid–air tri-phase interface. Due to the excellent conductivity and electrochemical activity of exfoliated $Ti_3C_2T_x$, $Ti_3C_2T_x$/PB composites greatly improved electrochemical performance compared to graphene/Prussian blue (PB) and carbon nanotubes (CNTs)/PB composites toward hydrogen peroxide detection. All active sensors (for glucose, lactate, and pH value) are independent and replaceable modules in the sensor platform, in which sensors can be inserted and replaced by the desired biomarker to detect. The substrates of these active sensors were prepared by superhydrophobic carbon fiber to create a tri-phase interface and protect the connector inside the sensor patch from sweat corrosion. The unique tri-phase interface design ensures a sufficient supply of O_2 and increases the stability of biosensors. The wearable sensing patch has been tested on human subjects for in vitro perspiration monitoring and showed that glucose and lactate could be measured simultaneously with high sensitivity and acceptable repeatability.

2. Results and Discussion

2.1. System Design of the Wearable Multifunctional Biosensing Patch

The multifunctional biosensing system must be compact and wearable, stable in its function, and highly durable. For unavoidable inactivation of enzymes and mechanical friction, a replaceable sensor component could be an effective strategy to prolong the service life of the wearable sensor. These requirements motivate a flexible modular biosensing patch that can be worn on the wrist with replaceable sensors. The patch-type wearable device that **Figure 1** schematically depicts has a

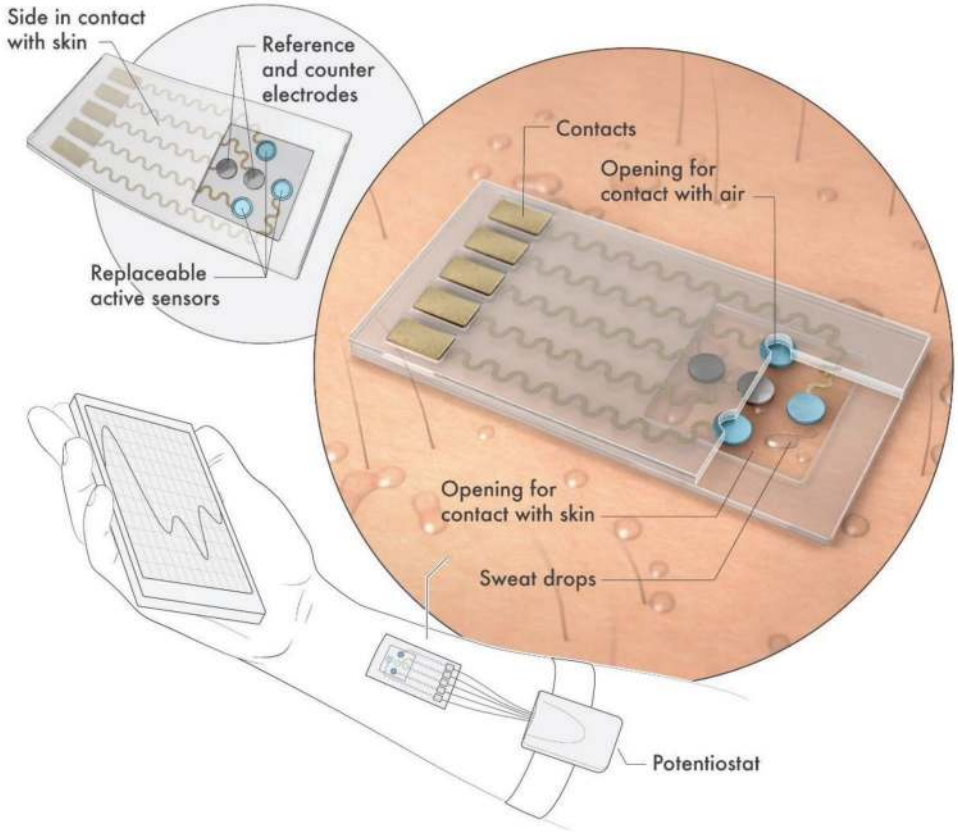

Figure 1. Schematic diagram of the sensor system.

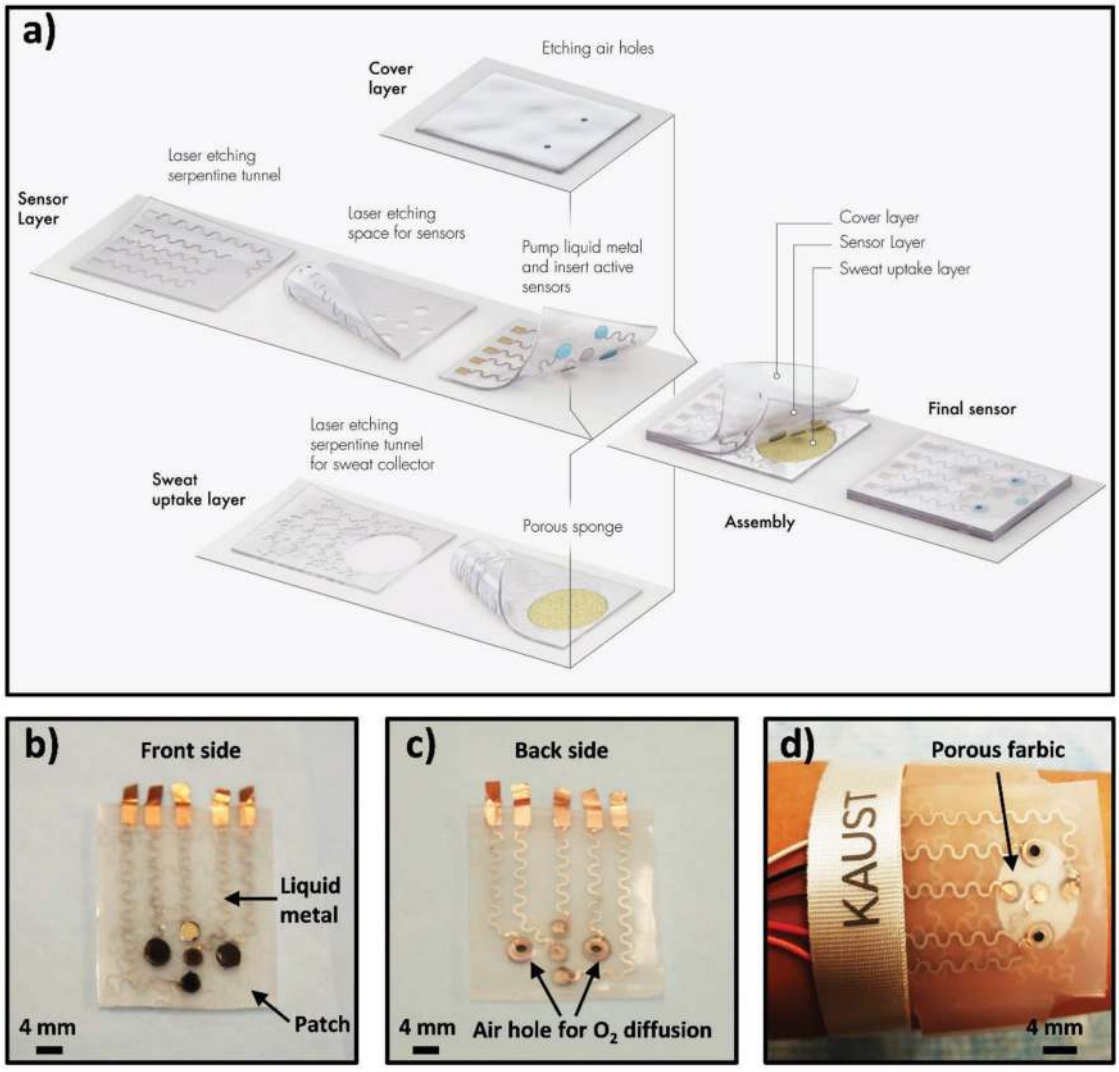

Figure 2. Schematic drawings and corresponding images of the wearable biosensor patch. a) Schematic illustration of the sensor patch system, which is composed of a sweat-uptake layer, a sensor layer, and a cover layer. b) Front-side optical image of the sensor array (left and right), reference electrode (top), counter electrode (middle), and pH sensor (bottom). c) Back-side optical image of the sensor array. d) Optical images of the sensor wristband laminated on human skin.

skin-conforming and stretchable design, which enables conformal contact with the skin for efficient sweat collection and high performance under physical deformation. All active sensors (glucose, lactate, and pH) along with the counter electrode and reference electrode are placed in independent and replaceable modules (**Figure 2**b). Therefore, if an electrode is used, expired or damaged, a replacement "insert" can simply be dropped into place in the sensor platform. Moreover, it will be easier to switch the production line from one analyte to the next in a manufacturing environment, as Figure S1 (Supporting Information) illustrates. After wearing the patch, sweat accumulates in the sweat-uptake layer. The glucose, lactate, and pH sensors begin to conduct measurements to determine sweat glucose, lactate, and pH levels. The measured pH value is then used to adjust the glucose and lactate concentrations through the calibration plot at different pH values (Figure S12, Supporting Information).

The integrated system (Figure 2a) consists of three modules: a sweat-uptake layer, a sensor layer (glucose, lactate, and pH sensors), and a cover layer. The sweat-uptake layer is composed of serpentine tunnels and a porous fabric for sweat collection (Figure S1, Supporting Information). Five sensor spaces and serpentine tunnels were etched onto the sensor layer for inserting active sensors (Figure S1, Supporting Information). The cover layer was produced from soft silicone rubber in which air holes were intentionally introduced to allow oxygen to easily diffuse from the air through the holes and toward the active sensor layer (Figure 2c). After assembling the cover layer with the sensor layer, liquid metal (made from the nontoxic liquid-metal alloy Galinstan) was pumped into the serpentine sealed tunnels (Figure S1, Supporting Information). This resulted in a multifunctional biosensor with high conductivity and mechanical stretchability for stable electrical signal transfer in the large-area wearable device configuration. All modules

were prepared from the highly flexible and stretchable Ecoflex sheet, which ensures mechanical reliability and a semi-transparent, skin-like appearance in the wearable device.

Moreover, soft material with a stretchable design provides extremely conformal contacts to the human skin under deformation without prompting any discomfort. The serpentine liquid metal wire in sealed tunnels strongly enhanced the electrical conductivity (less than 0.3 Ω; see Figure S2, Supporting Information) in comparison to vapor phase deposition graphene and screen-printing electrodes, and it minimized mechanical fractures during a cyclic stretching test[40] (Figure S2, Supporting Information). The Ecoflex band can be assembled on the patch to yield a wristband device that offers adequate access to perspiration for electrochemical measurements (Figure 2d). Figure 5a provides details of the system integration and operations, including portable and wireless units.

2.2. Material Strategy and Characterization of the $Ti_3C_2T_x$/PB Nanocomposite

The electrochemical detection platform is based on the use of $Ti_3C_2T_x$ MXene. A $Ti_3C_2T_x$/PB composite was employed as an electrochemical indicator to monitor the detection and as a catalyst for the selective reduction of hydrogen peroxide (Figure S10, Supporting Information) at a typical working voltage of −0.1V (vs Ag/AgCl). $Ti_3C_2T_x$ was synthesized with the minimal intensive layer delamination method, by manual shaking of the $Ti_3C_2T_x$ powder suspension in water to achieve delamination. This method yielded a stable aqueous colloidal solution of $Ti_3C_2T_x$. The Supporting Information contains synthesis details, while **Figure 3**b displays the morphologies of the $Ti_3C_2T_x$ nanosheets. The $Ti_3C_2T_x$ nanosheet is around 4 µm in size. Figure 3c presents the transmission electron micrographs of $Ti_3C_2T_x$/PB, the synthesis of which is described in the Supporting Information. Shape-controlled and well-dispersed PB nanoparticles (≈30 nm) were dispersed on the $Ti_3C_2T_x$ nanosheet surface (Figure 3d).

The size, dispersion, and concentration of the PB nanoparticles vary according to experimental conditions, especially (a) the molar ratio of $Ti_3C_2T_x$ and PB precursor ($K_3Fe(CN)_6$), (b) reaction temperature, and (c) reaction time. To obtain shape-controlled and well-dispersed $Ti_3C_2T_x$/PB nanocomposites, a series of experiments was designed to synthesize the expected nanohybrids. The Supporting Information elaborates on the synthesis procedures. In addition, Raman, X-ray diffraction (XRD), and atomic force microscopy (AFM) measurements were performed to characterize the morphology, crystal structure, and composition of the $Ti_3C_2T_x$ nanosheets and $Ti_3C_2T_x$/PB composite. Figure S7 (Supporting Information) conveys the XRD patterns of pure $Ti_3C_2T_x$ nanosheets, PB nanoparticles, and $Ti_3C_2T_x$/PB composites. The black trace represents $Ti_3C_2T_x$ nanosheets and exhibits a sharp, intense peak (002) at 2θ of 7.1°, which corresponds to d-spacing of 1.24 nm. The disappearance of the diffraction signal in the out-of-plane direction suggests the full exfoliation of $Ti_3C_2T_x$ without crystallographic stacking of $Ti_3C_2T_x$ nanosheets. Meanwhile, the red trace symbolizes $Ti_3C_2T_x$/PB and illustrates diffraction peaks at 17.37, 24.88, 35.27, and 39.59, which can be respectively assigned to the (200), (220), (400), and (420) reflections of the PB nanoparticles (JCPDS card No. 73-0687). The (002) peak of $Ti_3C_2T_x$ at 7.1° (2θ) broadens, exhibits lower intensity, and shifts to 6.5° in the case of $Ti_3C_2T_x$/PB nanohybrids, which validates the formation of the nanocomposite. Intense peaks correspond to the (200), (220), (400), and (420) planes of the PB, which confirm the successful hybridization. Figure S7 (Supporting Information)

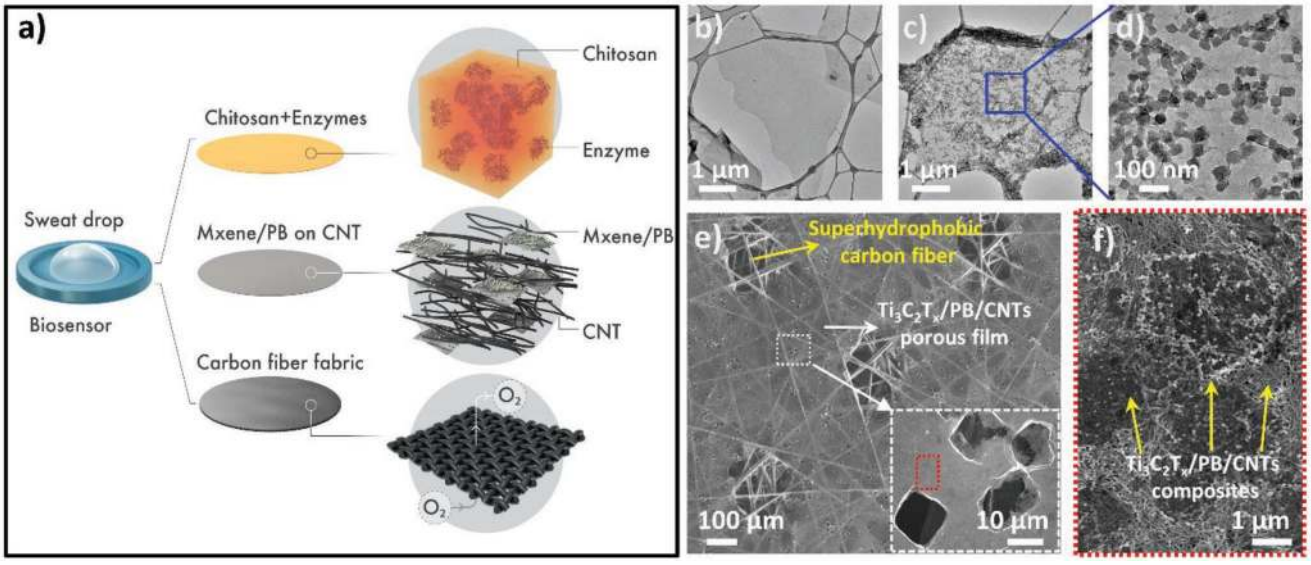

Figure 3. a) Schematic illustration of the oxygen-rich enzyme electrode. b) Transmission electron microscopy images of $Ti_3C_2T_x$ nanosheets. c,d) Transmission electron microscopy images of the $Ti_3C_2T_x$/PB composite. e) Scanning electron microscopy image of porous and ultrathin $Ti_3C_2T_x$/PB and CNTs ternary film, with the inset (white box) displaying a zoomed-in scanning electron microscopy image of the holes in the film. f) Magnified image of the region marked by a red frame in (e), which depicts the porous and ultrathin $Ti_3C_2T_x$/PB and CNTs ternary film.

contains Raman spectra of delaminated $Ti_3C_2T_x$ nanosheets, PB nanoparticles, and $Ti_3C_2T_x$/PB nanocomposites. Finally, the blue trace signifies the $Ti_3C_2T_x$/PB composite. Typical signatures of $Ti_3C_2T_x$ are observed at 204, 376, and 578 cm^{-1}, and signatures of PB at around 272, 2,092, and 2,155 cm^{-1}, which further confirmed the successful synthesis of $Ti_3C_2T_x$/PB composites.[41–43] As indicated from the AFM measurements (Figure S8, Supporting Information), the $Ti_3C_2T_x$ nanosheet has a uniform thickness of 1.8 nm, which includes trapped water molecules between the flake and the substrate.[19] The step height at the edge of the $Ti_3C_2T_x$/PB flake shown in Figure S8 (Supporting Information) is about 3.7 nm, which represents a two-layer $Ti_3C_2T_x$ nanosheet. The peaks in the height profile of the nanocomposite correspond to the well-dispersed PB nanoparticles on $Ti_3C_2T_x$ nanosheet.

2.3. Oxygen-Rich Electrode Design with a Three-Phase Interface

CNTs are promising for the reinforcement of interlaminar composites due to their extraordinary mechanical and physical properties.[44] They are also effective for improving multifunctional characteristics, including electrical and thermal conductivities of laminated composites.[45] Superhydrophobic carbon fiber membranes (CFMs) are commercially available and are as attractive as candidates as flexible electrodes, as they offer high electrical conductivity, chemical stability, and high permeability. Moreover, CFMs display adequate superhydrophobic properties, which prevent water from wetting (see Figure S4, Supporting Information), which renders them suitable for the construction of a three-phase interface. Based on such attractive features, we added CNTs to our $Ti_3C_2T_x$/PB composite to enforce mechanical stability. The CNTs-intercalated $Ti_3C_2T_x$/PB ultrathin laminar film (≈200 nm; Figure S7, Supporting Information) was then transferred onto CFMs to facilitate oxygen diffusion.

Figure 3a schematically depicts the oxygen-rich electrode with a solid–liquid–air three-phase interface. The oxygen-rich electrode in this work consisted of CNTs-intercalated $Ti_3C_2T_x$/PB ultrathin porous laminar film and a conducting superhydrophobic carbon fiber bottom layer (CNTs/$Ti_3C_2T_x$/PB/CFMs). The Experimental Section recounts the preparation process, which Figure 3e visualizes. A certain mass ratio (typically between 1:20 and 1:100) of CNTs and $CaCO_3$ particles (≈15 µm; Figure S3, Supporting Information) was added to the as-prepared $Ti_3C_2T_x$/PB nanohybrids to form a dispersion. Then, the CNTs-intercalated $Ti_3C_2T_x$/PB ultrathin laminar film was assembled by vacuum filtration of a specific amount of the dispersion on a mixed cellulose ester (MCE) filter membrane (Figure S3, Supporting Information). The $CaCO_3$ particles were then dissolved through the use of 0.1 M HCl to obtain small pores of the film, which facilitate the penetration of O_2 (inset of Figure 3e; Figure S3, Supporting Information). Finally, the ultrathin film was transferred to superhydrophobic CFMs and dried at room temperature. After dropping the mixed oxidase solution onto the prepared CNTs/$Ti_3C_2T_x$/PB/CFMs electrode and drying, the enzyme electrodes were obtained.

Dropping the mixed oxidase solution onto the CNTs/$Ti_3C_2T_x$/PB/CFMs electrode reveals misfit stress between the precipitate crystal and the ultrathin film. Such stress can cause the film to crack (Figure S4, Supporting Information). Thus, laser cutting was employed to introduce the large pores (≈200 µm) on the surface of the ultrathin film and release the misfit stress (Figure S3, Supporting Information). During the electrode fabrication process, $Ti_3C_2T_x$/PB hybrid nanosheets were interlocked with each other, and CNTs were intertwined, thereby forming the nest-like structures in the restacked $Ti_3C_2T_x$/PB layers. This established corrugations and nanopores to achieve larger surface-active sites and a beneficial effect on enzyme immobilization (Figure 3f). This porous and ultrathin structure significantly improved sensitivity as well as the reliability of the composites under mechanical friction and deformation.

Combining this porous upper layer with the CFM bottom layer formed a superhydrophobic electrode with a solid–liquid–air three-phase interface where oxygen is sufficient and constant, as the previous research has reported.[46] The contact of such electrode to the analyte solution creates a solid–liquid–air tri-phase interface that allows oxygen to diffuse directly from the air phase at the bottom of the electrode to the respective enzyme. Given that the diffusion coefficient of oxygen in the air phase (2.0×10^{-1} cm^2 s^{-1}) is much higher than that in the liquid phase (2.1×10^{-5} cm^2 s^{-1}),[38] the oxygen level at the tri-phase reaction zone remains relatively constant and can be several orders of magnitude higher. An oxygen-rich enzyme electrode ensures fast analyte delivery and the formation of an abundant quantity of H_2O_2, which in turn strengthens the signal and permits a more precise assay.

The electrochemical properties of the as-prepared CNTs/$Ti_3C_2T_x$/PB/CFMs sensor were measured, and Figure S9 (Supporting Information) depicts the cyclic voltammetry that was recorded at different scan rates at the CNTs/$Ti_3C_2T_x$/PB/CFMs electrode in 0.1 M KCl solution. Evidently, the peak currents became proportional to the square root of the scan rate (Figure S9, Supporting Information), which indicates diffusion-controlled processes. Figure S9 (Supporting Information) provides the highly reproducible chronoamperometric response of the CNTs/$Ti_3C_2T_x$/PB/CFMs H_2O_2 electrode to H_2O_2 after incremental additions of H_2O_2 without interruption. The calibration plot in Figure S9 (Supporting Information) illustrates that the linear detection range extends from as low as 200×10^{-9} M to 4.8×10^{-3} M ($R^2 = 0.999$), with a detection limit of 67×10^{-9} M at a signal-to-noise (S/N) ratio of 3.

To assess the analytical performance level of the H_2O_2 sensor, control experiments were conducted to compare the H_2O_2 sensing performance of our sensor with typical graphene/PB and CNTs/PB composites-based sensor (preparation details are provided in the Supporting Information). The sensitivity of MXene/PB-based H_2O_2 sensor (52.3 µA mM^{-1}) is largely increased as compared to CNTs/PB (40.5 µA mM^{-1}) and graphene/PB (29.7 µA mM^{-1}) (Figure S13, Supporting Information). Moreover, the characteristic features of the H_2O_2 sensor were compared to other PB-based H_2O_2 sensors (see Table S1, Supporting Information). Such comparison revealed that the sensor we introduce exhibited improved electrochemical performance in terms of linearity, detection limit, and sensitivity when compared to previously reported models toward H_2O_2 reduction. The high sensitivity (408.3 µA mM^{-1} cm^{-2}) in turn yields in a low detection limit. The excellent conductivity and

activity of $Ti_3C_2T_x$ as well as the porous structure with a triphase interface all contribute to enhanced linearity, sensitivity, and accuracy.

2.4. Electrochemical Characterization of Individual Sensors

The oxygen-rich biosensors were prepared by immobilizing the respective oxidase on the porous and ultrathin CNTs/$Ti_3C_2T_x$/PB/CFMs electrode. The prepared electrodes were then inserted into the sensor platform at the positions of the blue circular disks in Figure 1.

The glucose sensor consisted of a CNTs/$Ti_3C_2T_x$/PB/CFMs electrode that was modified with the enzyme glucose oxidase (Gox). It was calibrated by using artificial sweat with glucose in concentrations that ranged from 10×10^{-6} M to 1.5×10^{-3} M. The detection sensitivity was 35.3 μA mM^{-1} cm^{-2}, as determined by chronoamperometry (**Figure 4**a). The inset in Figure 4a

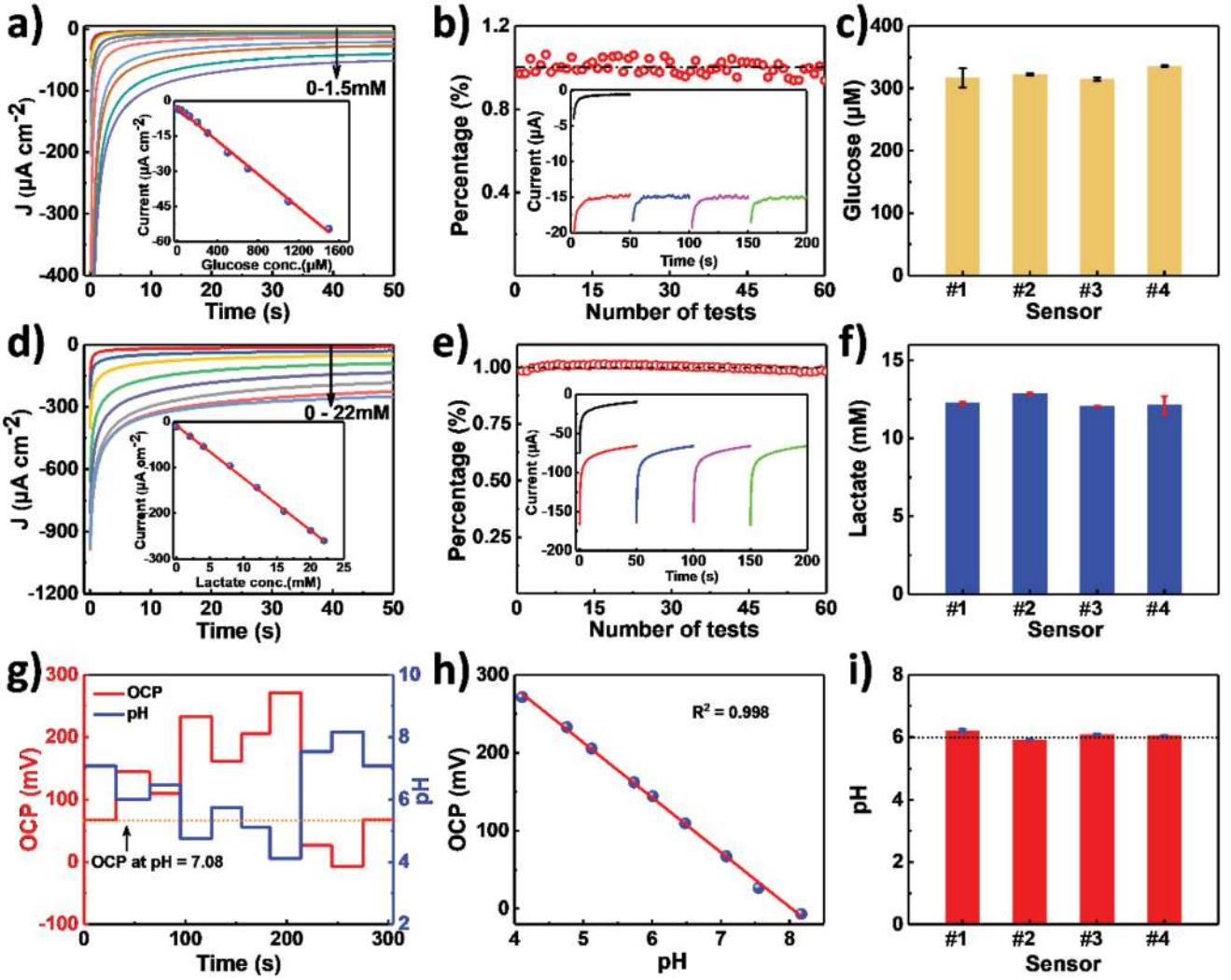

Figure 4. a) Chronoamperometric response of the glucose sensor to increasing glucose concentrations from 0 to 1.5×10^{-3} M in phosphate-buffered saline (pH = 6), with the inset displaying a calibration curve of the glucose sensor based on sampling the current at 30 s. b) Typical chronoamperometric responses of the glucose sensor as a function of time with 60 iterations, with the inset figure displaying the chronoamperometric response at 10th, 20th, 30th, and 40th tests; relative responses (%) were calculated by normalizing the current to the initial current obtained at 30 s following the potential step. c) Chronoamperometric response of the same batch of glucose sensors obtained at 30 s in phosphate-buffered saline with 300×10^{-6} M glucose to check the repeatability of sensors. d) Chronoamperometric response of the lactate sensor to increasing lactate concentrations from 0 to 22×10^{-3} M in phosphate-buffered saline (pH = 6.0), with the inset displaying a calibration curve of the lactate sensor based on sampling the current at 30 s. e) Typical chronoamperometric responses of lactate sensor as a function of time with 60 iterations, with the inset figure displaying the chronoamperometric response at 10th, 20th, 30th, and 40th tests; relative responses (%) were calculated by normalizing the current to the initial current obtained at 30 s following the potential step. f) Chronoamperometric response of the same batch of lactate sensors obtained at 30 s in phosphate-buffered saline with 12×10^{-3} M lactate to check the repeatability of sensors. g) Open circuit potential changes of the pH sensor and the performance of the pH sensor in standard buffered solutions whose pH changes were 7.08→6.01→6.48→4.76→5.74→5.12→4.11→7.55→8.17→7.08 (dotted line, COP at pH = 7.08). h) Calibration curve of the pH sensor. i) Measured pH levels of the same batch of pH sensors in phosphate-buffered solution at pH = 6.0 (dotted line, pH levels measured by commercial pH assay).

contains the calibration plot. The detection limit of the glucose sensor is 0.33×10^{-6} M at a S/N ratio of 3 (Figure S10, Supporting Information). The glucose concentrations in sweat reflect glucose levels of hypoglycemic, hyperglycemic, and healthy people.[47–49]

The lactate sensor is also based on the use of a CNTs/$Ti_3C_2T_x$/PB/CFMs electrode that was modified with the enzyme lactate oxidase. It was calibrated through the use of artificial sweat with lactate in concentrations that ranged from 0×10^{-3} M to 22×10^{-3} M (typical human lactate concentrations in arm sweat)[51,53] with high electrochemical sensitivity (11.4 μA mM^{-1} cm^{-2}), as determined by chronoamperometry. The inset of Figure 4d presents the calibration plot. The detection limit of the lactate sensor is 0.67×10^{-6} M at a S/N ratio of 3 (Figure S10, Supporting Information). Figure 4b,e lists 60 successive measurements of 1×10^{-3} M glucose and 15×10^{-3} M lactate, respectively, using the same biosensor. Relative standard deviations (RSDs) of 5% and 1.9% were observed for these measurements. It is worth noting that the net currents of the signals (insets of Figure 4b,e) are substantially higher compared to the previously reported wearable sensor patches. This would reduce any interference by electromagnetic fields or background noise as well as enhance the sensitivity.

To assess the analytical performance of the sensor patch, characteristic features of the sensor were compared to other wearable sensor arrays (see Table S2, Supporting Information). The sensor arrays that we introduce exhibit improved electrochemical performance in terms of detection limit and sensitivity when compared to previously reported models toward glucose and lactate detection in human sweat.

Four glucose/lactate electrodes were randomly selected from a batch of samples and tested under the same experimental condition in three iterations. The RSDs of the glucose and lactate biosensor toward 300×10^{-6} M glucose and 12×10^{-3} M lactate were 4.8% and 4.7%, respectively, as Figure 4c,f demonstrates. The RSDs for electrode-to-electrode reproducibility of four electrodes that were tested under the same conditions were 2.9% and 3.0%, respectively. These results indicate a high reproducibility of these sensors, which suggests that this sensing platform can utilize them as replaceable inserts.

Selectivity tests were performed to examine the effects of other common interfering species that exist in human sweat. The performance of the glucose sensor was not compromised in the presence of ascorbic acid, uric acid, and lactic acid (Figure S11, Supporting Information) in concentration values that are typically found in sweat. Similarly, ascorbic acid, uric acid, and glucose did not interfere with the lactate sensor (Figure S11, Supporting Information). The glucose (with 200×10^{-6} M glucose) and lactate sensors (with 6×10^{-3} M lactate) functioned for several days without additional calibration under ambient conditions (Figure S12, Supporting Information).

The actual pH value strongly affects the performance of enzyme-based sensors (Figure S12, Supporting Information). Thus, simultaneous monitoring of pH values can enhance the accuracy of such sensors. The pH sensor is based on an ion-selective electrode (ISE) that consists of polyaniline (PANI) coated working electrode (Figure S4, Supporting Information) and an Ag/AgCl reference electrode. It relies on the deprotonation of PANI and measures changes in the open circuit potential between an ISE and a reference electrode.[51] The pH sensor was tested on standard buffer solutions of varying pH and displayed acceptable reliability from repeated use at different pH levels (Figure 4g). The calibration plot of the pH sensor (Figure 4h) indicates a sensitivity of –70 mV pH^{-1} with good linearity ($R^2 = 0.998$). Four pH electrodes were randomly selected and tested under the same experimental condition in three iterations. The RSD of the pH sensor toward the buffer solution (pH = 6) was 0.8% for three successive measurements, while the RSD for electrode-to-electrode reproducibility of four electrodes was 2.0% when measured under the same conditions (Figure 4i). Simultaneous pH sensing can correct this pH-dependent deviation of the enzyme-based sensors.

The influences of oxygen diffusion on the detection accuracy of biosensors were also investigated. Before the assay of a 1×10^{-3} M glucose solution, oxygen in the analyte solution was purged by bubbling with argon for 30 min. Figure S11 (Supporting Information) reports that the current output of the sensor with an open-air hole was high and remained stable. However, if the air hole was sealed, the current output was low and fluctuated for nearly 20 min. From the calibration plot of current versus lactate concentration that Figure S11 (Supporting Information) contains, an increased linear detection range (up to 22×10^{-3} M) as well as higher sensitivity was achieved when the air hole was open.

Biosensors with a sealed air hole have only a solid–liquid two-phase interface, whereby oxygen is supplied through the liquid phase with a low diffusion coefficient and fluctuant concentration. Hence, the supply of oxygen that is required in the enzymatic reaction zone is limited in accordance with Fick's law, which restricts the upper detection limit, linearity, sensitivity, and accuracy. In contrast, biosensors with an open-air hole possess a tri-phase reaction interface to achieve an adequate and constant oxygen supply and, consequently, a significantly higher detection sensitivity.

2.5. In Vitro Perspiration Monitoring on a Human Subject

The promise of the wearable multifunctional biosensor patch was demonstrated by monitoring sweat during 10–30 min of intense cycling activity (**Figure 5**b). The wristband sweat sensor was connected to a portable electrochemical analyzer with an internally integrated power supply, which supplied power to the patch (Figure 5a). Real-time analysis was then wirelessly transmitted to a remote mobile device, such as a smartphone or a tablet computer, and finally displayed in a custom-developed cellphone application (Figure 1). It takes an average of 2 min for the sweat-uptake layer of the patch to collect sweat for measurements. When the sweat-uptake layer absorbs enough sweat, the glucose, lactate, and pH sensors measure their respective concentrations. The pH sensing improves the detection accuracy, and the patch can be used multiple times by replacing the sensor "inserts" and sweat collection film in the sweat-uptake layer (Figure S1, Supporting Information).

Over time, the heightened resistance to cycling caused the subject to exert an increasing level of effort in order to

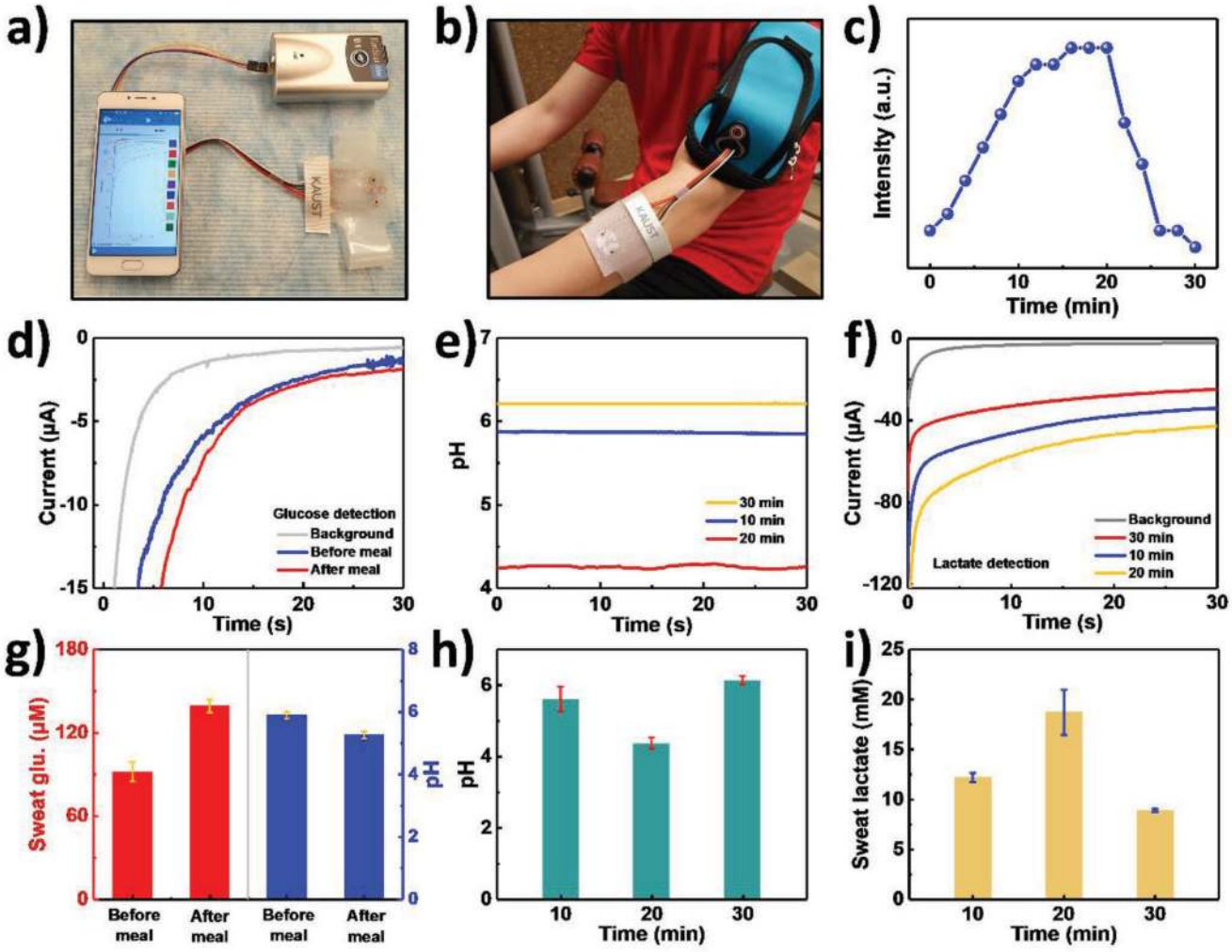

Figure 5. Real-time on-body evaluation of the sensor patch indicating the pH levels, lactate, and glucose concentrations. a) The wearable sweat-monitoring patch is connected to a portable electrochemical analyzer that supplies power and controls the patch and can wirelessly communicate with commercial mobile phones via Bluetooth. b) The wearable sweat-monitoring patch is connected to a portable electrochemical analyzer on the skin. c) Cycling resistance profile for on-body tests. d) Measured chronoamperometric responses of glucose sensors and pH changes before and after meals with three different glucose sensors. e) Measured pH level of pH sensor at different times during the exercise. f) Measured chronoamperometric responses of lactate sensor at different times during the exercise. g) Comparison of glucose and pH levels before and after meals with three different glucose and pH sensors. h) Comparison of pH levels at different times during the exercise with three different pH sensors. i) Comparison of lactate levels at different times during the exercise with three different lactate sensors.

maintain a constant cycling speed and resulted in the generation of sweat (Figure 5c). The measurements began when the sweat covered the working electrodes, the reference electrode, and the counter electrode. As the cycling resistance increased (20 min), the concentration of lactate in the sweat increased as well (Figure 5f,i), which suggests a correlation between physical exercise and after a physiological delay, lactate generation. The final stage of the cycling involved a 3 min cool-down period, at which point the lactate concentration that the biosensor measured diminished. This decrease was due to the sweat dilution factor phenomenon and the decreased cycling intensity.

The sweat pH levels also varied during physical movements (Figure 5e,h), which was mainly caused by the excretion of lactic acid. Both lactate and pH biosensor patch data for the subject resemble the expected sweat-lactate/pH profile for increasing workout intensity.[50] The sweat glucose values corrected for effects of pH before and after the consumption of two bananas agree well with reported blood and sweat glucose levels[53] (Figure 5d,g). Three glucose/lactate/pH working electrodes were inserted into the patch and exhibited acceptable repeatability.

The findings of these in vitro perspiration monitoring studies illustrate that our wearable multifunctional biosensor can simultaneously monitor sweat glucose, lactate, and pH. It also shows the MXenes-based biosensor maximizes enzyme activity. The data also demonstrate that three-phase interface design facilitates the supply of oxygen to the enzyme electrode, which allows for a larger linear detection range and ultrahigh sensitivity toward the biomarkers.

3. Conclusion

A wearable multifunctional sweat-based biosensor patch was developed incorporating $Ti_3C_2T_x$/PB composite for durable and sensitive detection of biomarkers in sweat. With unique 2D morphology and metallic conductivity of $Ti_3C_2T_x$, the $Ti_3C_2T_x$/PB composite shows distinctly improved electrochemical activity and stability for measuring hydrogen peroxide. The system integrates a skin-conforming stretchable biosensor with three replaceable sensor units into a single, on-body wearable platform. The access of oxygen to the enzymatically active layer is unlimited, which ensures maximized activity of the enzymes and results in a larger linear detection range, ultrahigh sensitivity, and accuracy toward the parameters of glucose and lactate. A pH sensor was also incorporated to account for variations in local pH values. The system outperformed previously reported graphene/PB and CNTs/PB-based biosensors, especially for in situ detection on human subjects. We believe that this work represents an essential step toward the realization of ultrasensitive enzymatic wearable biosensors for early disease identification and personalized health care.

4. Experimental Section

Fabrication Process of the Device Substrate: The wearable device fabrication began with CO_2 laser etching (10.6 µm) of the Ecoflex substrate (Ecoflex 00-30, silicone rubbers, Smooth-On, Inc. Homemade 1.0 mm film). The depth of the serpentine tunnels was about 0.3 mm on the sweat-uptake layer and 0.5 mm on the sensor layer, and the width of the tunnels on both layers was 0.8 mm. Two air holes with a diameter of 3 mm were fabricated via laser etching on the cover layer. After 10 min of ultraviolet treatment, the cover layer, sensor layer, and sweat-uptake layer were combined and exposed to 80 °C for 2 h and 100 °C for 1 h. Tiny copper foils with designed structures (0.1 mm, cut out by Yb fiber laser, 1.06 µm) were planted into the combined layers and worked as the wire connector. Liquid metal alloy (Changsha Santech Materials Co., Ltd, China) was then injected into microfluidic channels, which were located in the sensor layer, to form a stable microwire of liquid metal.

Preparation of Oxygen-Rich CNTs/$Ti_3C_2T_x$/PB/CFMs Electrode: The CNTs dispersion (CNTs, purity: >95%, XF Nano, Inc, China) was first prepared by mixing 50 mg of CNTs powder, 0.5 g of sodium dodecyl benzene sulfonate, and 500 mL of deionized water before sonicating the mixture for 24 h under a power of 2 kW. The as-prepared CNTs dispersion was centrifuged for 15 min at 12 000 rpm, and the supernatant solution (0.07 mg mL^{-1}) was collected for the following experiments. The CNTs/$Ti_3C_2T_x$/PB/$CaCO_3$ film was prepared via a wet process by which 120 µL of $Ti_3C_2T_x$/PB nanocomposite (1 mg mL^{-1}), 1 mL of homemade $CaCO_3$ particles suspension (3mg mL^{-1}), 2 mL of CNTs dispersion (0.07 mg mL^{-1}), and 200 mL of distilled water were mixed and filtered onto an MCE filter membrane (0.2 µm pore size and 4 cm diameter). The CNTs/$Ti_3C_2T_x$/PB/$CaCO_3$ film was cut into small circles with 6 mm diameters and 250 µm microholes on the surface by the CO_2 layer, and $CaCO_3$ particles were removed via acid etching (hydrochloric acid, 0.1 M) for 10 min to create the CNTs/$Ti_3C_2T_x$/PB porous film. This film was then released from the MCE filter membrane and transferred onto superhydrophobic carbon fiber paper (TGP-H-030, Fuel Cell Earth) to obtain the oxygen-rich CNTs/$Ti_3C_2T_x$/PB/CFMs electrode.

Preparation of Oxygen-Rich Glucose and Lactate Sensor: 2 mg mL^{-1} of chitosan (medium molecular weight, Sigma-Aldrich) solution was prepared by dissolving the chitosan in 2 wt% acetic acid (99%, Sigma-Aldrich). The chitosan solution was mixed with 25 mg mL^{-1} of Gox (2.07 U mg^{-1}; Sigma-Aldrich) in phosphate-buffered saline (pH = 7), bovine serum albumin (BSA) (10 mg mL^{-1} aqueous solution, Sigma-Aldrich), and diluted 1.0 wt% aqueous glutaraldehyde (Grade I, 25% in DI water, Sigma-Aldrich) with a volume ratio of 2:4:1:1. Then, 10 µL of the mixture was drop-casted onto the CNTs/$Ti_3C_2T_x$/PB/CFMs electrode followed by drying the electrodes under ambient conditions. The as-prepared sensors were stored in the refrigerator at 4 °C. For the lactate sensor, the 2 mg mL^{-1} chitosan solution was mixed with 30 mg mL^{-1} of lactate oxidase (80 U mg^{-1}; Creative Enzymes, USA) in phosphate-buffered saline (pH = 7), BSA (10 mg mL^{-1}), and diluted 1.0 wt% aqueous glutaraldehyde (Grade I, 25% in DI water, Sigma-Aldrich) with a volume ratio of 2:4:1:1. Subsequently, 20 µL of the mixture was drop-casted onto the CNTs/$Ti_3C_2T_x$/PB/CFMs electrode, which was dried under ambient conditions. The thickness of the enzyme layer was around 100 and 300 nm for the glucose and lactate sensor, respectively. The as-prepared sensors were stored in the refrigerator at 4 °C when they were not in use.

Preparation of pH Sensor: Carbon nanotube film was prepared via a wet process whereby 2 mL of CNTs dispersion (0.07 mg mL^{-1}) and 200 mL of distilled water were mixed and filtered onto an MCE filter membrane (0.2 µm pore size and 4 cm diameter). Then, the CNTs film was cut into small circles with 3 mm diameters by the CO_2 layer. This circular film was subsequently released from the MCE filter membrane and transferred onto superhydrophobic carbon fiber paper (TGP-H-030, Fuel Cell Earth). An aqueous solution of 0.1 M aniline (99.5%, Sigma-Aldrich) in 1 M of HCl was prepared. The CNTs/CFMs electrode was dipped into the solution, and the potential was swept from –0.2 to 1 V versus a commercial Ag/AgCl electrode for 40 segments at a scan rate of 0.1 V s^{-1}.

Preparation of Reference and Counter Electrodes: Ag/AgCl ink (product #011464, ALS Co., Ltd, Japan) was painted onto the superhydrophobic carbon fiber paper (diameter: 3 mm, TGP-H-030, Fuel Cell Earth) and oven-dried at 120 °C for ≈15 min. A platinum thin film (≈50 nm) was deposited onto the superhydrophobic carbon fiber paper (diameter: 3 mm) by sputtering for the counter electrode.

Supporting Information

Supporting Information is available from the Wiley Online Library or from the author.

Acknowledgements

The research reported in this manuscript was supported by funding from the King Abdullah University of Science and Technology (KAUST) under the Sensors Initiative (CRF-2015-SENSORS-2709). The authors thank the Advanced Nanofabrication, Imaging and Characterization Laboratory at KAUST for their excellent support. Y.L. thanks the help from Dr. Yunpei Zhu (KAUST) and Dr. Kang Hyuck Lee (KAUST). Figures 1,2a, and 3a were produced by Xavier Pita, a scientific illustrator at the King Abdullah University of Science and Technology (KAUST).

Conflict of Interest

The authors declare no conflict of interest.

Keywords

biosensor, MXene, perspiration analysis, wearable device

Received: March 5, 2019
Revised: March 25, 2019
Published online:

[1] Y. Khan, A. E. Ostfeld, C. M. Lochner, A. Pierre, A. C. Arias, *Adv. Mater.* **2016**, *28*, 4373.
[2] Y.-Z. Zhang, K. H. Lee, D. H. Anjum, R. Sougrat, Q. Jiang, H. Kim, H. N. Alshareef, *Sci. Adv.* **2018**, *4*, eaat0098.
[3] D. Son, J. Lee, S. Qiao, R. Ghaffari, J. Kim, J. E. Lee, C. Song, S. J. Kim, D. J. Lee, S. W. Jun, S. Yang, M. Park, J. Shin, K. Do, M. Lee, K. Kang, C. S. Hwang, N. Lu, T. Hyeon, D.-H. Kim, *Nat. Nanotechnol.* **2014**, *9*, 397.
[4] W. Gao, S. Emaminejad, H. Y. Y. Nyein, S. Challa, K. Chen, A. Peck, H. M. Fahad, H. Ota, H. Shiraki, D. Kiriya, D.-H. Lien, G. A. Brooks, R. W. Davis, A. Javey, *Nature* **2016**, *529*, 509.
[5] S. Imani, A. J. Bandodkar, A. M. V. Mohan, R. Kumar, S. Yu, J. Wang, P. P. Mercier, *Nat. Commun.* **2016**, *7*, 11650.
[6] H. Lee, T. K. Choi, Y. B. Lee, H. R. Cho, R. Ghaffari, L. Wang, H. J. Choi, T. D. Chung, N. Lu, T. Hyeon, S. H. Choi, D.-H. Kim, *Nat. Nanotechnol.* **2016**, *11*, 566.
[7] H. Lee, C. Song, Y. S. Hong, M. S. Kim, H. R. Cho, T. Kang, K. Shin, S. H. Choi, T. Hyeon, D.-H. Kim, *Sci. Adv.* **2017**, *3*, e1601314.
[8] A. J. Bandodkar, W. Jia, C. Yardimci, X. Wang, J. Ramirez, J. Wang, *Anal. Chem.* **2015**, *87*, 394.
[9] W. Jia, A. J. Bandodkar, G. Valdés-Ramírez, J. R. Windmiller, Z. Yang, J. Ramírez, G. Chan, J. Wang, *Anal. Chem.* **2013**, *85*, 6553.
[10] J. Y. Oh, S. Rondeau-Gagné, Y.-C. Chiu, A. Chortos, F. Lissel, G.-J. N. Wang, B. C. Schroeder, T. Kurosawa, J. Lopez, T. Katsumata, J. Xu, C. Zhu, X. Gu, W.-G. Bae, Y. Kim, L. Jin, J. W. Chung, J. B.-H. Tok, Z. Bao, *Nature* **2016**, *539*, 411.
[11] H. Tang, F. Yan, P. Lin, J. Xu, H. L. W. Chan, *Adv. Funct. Mater.* **2011**, *21*, 2264.
[12] C. Liao, M. Zhang, M. Y. Yao, T. Hua, L. Li, F. Feng, *Adv. Mater.* **2015**, *27*, 7493.
[13] C. Liao, C. Mark, M. Zhang, H. L. W. Chan, F. Yan, *Adv. Mater.* **2015**, *27*, 676.
[14] K. S. Kim, Y. Zhao, H. Jang, S. Y. Lee, J. M. Kim, K. S. Kim, J.-H. Ahn, P. Kim, J.-Y. Choi, B. H. Hong, *Nature* **2009**, *457*, 706.
[15] B. Anasori, M. R. Lukatskaya, Y. Gogotsi, *Nat. Rev. Mater.* **2017**, *2*, 16098.
[16] M. Naguib, V. N. Mochalin, M. W. Barsoum, Y. Gogotsi, *Adv. Mater.* **2014**, *26*, 992.
[17] K. Huang, Z. Li, J. Lin, G. Han, P. Huang, *Chem. Soc. Rev.* **2018**, *47*, 5109.
[18] F. Shahzad, M. Alhabeb, C. B. Hatter, B. Anasori, S. M. Hong, C. M. Koo, Y. Gogotsi, *Science* **2016**, *353*, 1137.
[19] M. R. Lukatskaya, O. Mashtalir, C. E. Ren, Y. Dall'Agnese, P. Rozier, P. L. Taberna, M. Naguib, P. Simon, M. W. Barsoum, Y. Gogotsi, *Science* **2013**, *341*, 1502.
[20] M. R. Lukatskaya, S. Kota, Z. Lin, M.-Q. Zhao, N. Shpigel, M. D. Levi, J. Halim, P.-L. Taberna, M. W. Barsoum, P. Simon, Y. Gogotsi, *Nat. Energy* **2017**, *2*, 17105.
[21] S. Niu, Z. Wang, M. Yu, M. Yu, L. Xiu, S. Wang, X. Wu, J. Qiu, *ACS Nano* **2018**, *12*, 3928.
[22] J. Yan, C. E. Ren, K. Maleski, C. B. Hatter, B. Anasori, P. Urbankowski, A. Sarycheva, Y. Gogotsi, *Adv. Funct. Mater.* **2017**, *27*, 1701264.
[23] J. Ran, G. Gao, F.-T. Li, T.-Y. Ma, A. Du, S.-Z. Qiao, *Nat. Commun.* **2017**, *8*, 13907.
[24] Y. Ma, N. Liu, L. Li, X. Hu, Z. Zou, J. Wang, S. Luo, Y. Gao, *Nat. Commun.* **2017**, *8*, 1207.
[25] Y. Ma, Y. Yue, H. Zhang, F. Cheng, W. Zhao, J. Rao, S. Luo, J. Wang, X. Jiang, Z. Liu, N. Liu, Y. Gao, *ACS Nano* **2018**, *12*, 3209.
[26] F. Wang, C. H. Yang, M. Duan, Y. Tang, J. F. Zhu, *Biosens. Bioelectron.* **2015**, *74*, 1022.
[27] S. Chertopalov, V. N. Mochalin, *ACS Nano* **2018**, *12*, 6109.
[28] R. B. Rakhi, P. Nayak, C. Xia, H. N. Alshareef, *Sci. Rep.* **2016**, *6*, 36422.
[29] B. Xu, M. Zhu, W. Zhang, X. Zhen, Z. Pei, Q. Xue, C. Zhi, P. Shi, *Adv. Mater.* **2016**, *28*, 3333.
[30] C. Tan, X. Cao, X.-J. Wu, Q. He, J. Yang, X. Zhang, J. Chen, W. Zhao, S. Han, G.-H. Nam, M. Sindoro, H. Zhang, *Chem. Rev.* **2017**, *117*, 6225.
[31] A. Sinha, Dhanjai, H. Zhao, Y. Huang, X. Lu, J. Chen, R. Jain, *Trends Anal. Chem.* **2018**, *105*, 424.
[32] L. Wu, X. Lu, Dhanjai, Z.-S. Wu, Y. Dong, X. Wang, S. Zheng, J. Chen, *Biosens. Bioelectron.* **2018**, *107*, 69.
[33] P. Nayak, Q. Jiang, R. Mohanraman, D. Anjum, M. N. Hedhili, H. N. Alshareef, *Nanoscale* **2018**, *10*, 17030.
[34] M. R. Romero, F. Ahumada, F. Garay, A. M. Baruzzi, *Anal. Chem.* **2010**, *82*, 5568.
[35] J. Wang, *Chem. Rev.* **2008**, *108*, 814.
[36] J. Kim, I. Jeerapan, S. Imani, T. N. Cho, A. Bandodkar, S. Cinti, P. P. Mercier, J. Wang, *ACS Sens.* **2016**, *1*, 1011.
[37] A. N. Sekretaryova, V. Beni, M. Eriksson, A. A. Karyakin, A. P. F. Turner, M. Y. Vagin, *Anal. Chem.* **2014**, *86*, 9540.
[38] E. L. Cussler, *Diffusion: Mass Transfer in Fluid Systems*, Cambridge University Press, Cambridge, UK **2009**.
[39] Y. Lei, R. Sun, X. Zhang, X. Feng, L. Jiang, *Adv. Mater.* **2016**, *28*, 1477.
[40] A. J. Bandodkar, R. Nuñez-Flores, W. Jia, J. Wang, *Adv. Mater.* **2015**, *27*, 3060.
[41] S. Su, X. Han, Z. Lu, W. Liu, D. Zhu, J. Chao, C. Fan, L. Wang, S. Song, L. Weng, L. Wang, *ACS Appl. Mater. Interfaces* **2017**, *9*, 12773.
[42] T. Hu, J. Wang, H. Zhang, Z. Li, M. Hu, X. Wang, *Phys. Chem. Chem. Phys.* **2015**, *17*, 9997.
[43] G. Moretti, C. Gervais, *J. Raman Spectrosc.* **2018**, *49*, 1198.
[44] V. P. Veedu, A. Cao, X. Li, K. Ma, C. Soldano, S. Kar, P. M. Ajayan, M. N. Ghasemi-Nejhad, *Nat. Mater.* **2006**, *5*, 457.
[45] E. T. Thostenson, T.-W. Chou, *Adv. Mater.* **2006**, *18*, 2837.
[46] Z. Song, C. Xu, X. Sheng, X. Feng, L. Jiang, *Adv. Mater.* **2018**, *30*, 1701473.
[47] K. Sakaguchi, Y. Hirota, N. Hashimoto, W. Ogawa, T. Hamaguchi, T. Matsuo, J.-I. Miyagawa, M. Namba, T. Sato, S. Okada, K. Tomita, M. Matsuhisa, H. Kaneto, K. Kosugi, H. Maegawa, H. Nakajima, A. Kashiwagi, *J. Diabetes Sci. Technol.* **2013**, *7*, 678.
[48] J. Moyer, D. Wilson, I. Finkelshtein, B. Wong, R. Potts, *Diabetes Technol. Ther.* **2012**, *14*, 398.
[49] M. J. Patterson, S. D. R. Galloway, M. A. Nimmo, *Exp. Physiol.* **2000**, *85*, 869.
[50] R. Rahimi, M. Ochoa, A. Tamayol, S. Khalili, A. Khademhosseini, B. Ziaie, *ACS Appl. Mater. Interfaces* **2017**, *9*, 9015.
[51] M. J. Buono, N. V. L. Lee, P. W. Miller, *J. Physiol. Sci.* **2010**, *60*, 103.
[52] A. Martín, J. Kim, J. F. Kurniawan, J. R. Sempionatto, J. R. Moreto, G. Tang, A. S. Campbell, A. Shin, M. Y. Lee, X. Liu, J. Wang, *ACS Sens.* **2017**, *2*, 1860.
[53] J. M. Green, R. C. Pritchett, T. R. Crews, J. R. McLester Jr., D. C. Tucker, *Eur. J. Appl. Physiol.* **2004**, *91*, 1.

